frontiers | Frontiers in Earth Science

TYPE Original Research
PUBLISHED 19 November 2024
DOI 10.3389/feart.2024.1502160

OPEN ACCESS

EDITED BY
Hongjian Zhu,
Yanshan University, China

REVIEWED BY
Ubedullah Ansari,
Mehran University of Engineering and Technology, Pakistan
Zhonghong Chen,
China University of Petroleum, China
Kai Wang,
University of Oklahoma, United States

*CORRESPONDENCE
Peng Sun,
p_sun@yangtzeu.edu.cn

RECEIVED 26 September 2024
ACCEPTED 22 October 2024
PUBLISHED 19 November 2024

CITATION
Liu T, Zhang W, Chen C, Shen H, Shao W and Sun P (2024) Controlling factors of fluid mobility in the tuff reservoirs of the Huoshiling formation, Dehui fault depression, southeastern Songliao Basin: insights from micro-nano pore structures.
Front. Earth Sci. 12:1502160.
doi: 10.3389/feart.2024.1502160

Controlling factors of fluid mobility in the tuff reservoirs of the Huoshiling formation, Dehui fault depression, southeastern Songliao Basin: insights from micro-nano pore structures

Tianfu Liu[1,2], Wei Zhang[3], Chong Chen[4], Huaiming Shen[4], Wenjie Shao[5] and Peng Sun[6,7]*

[1]PetroChina Usmile Company Limited, Beijing, China, [2]School of Economics and Management, Northeast Petroleum University, Daqing, Heilongjiang, China, [3]North China Branch, China National Logging Corporation, Renqiu, Hebei, China, [4]The Six Geological Party, Tibet Bureau of Geological and Mineral Exploration and Development, Lasa, Xizang, China, [5]Henan Fifth Geological Exploration Institute Co., Ltd., Zhengzhou, Henan, China, [6]School of Petroleum Engineering, Yangtze University, Wuhan, China, [7]Hubei Key Laboratory of Petroleum Geochemistry and Environment, Yangtze University, Wuhan, China

This study addresses the unclear understanding of the primary factors controlling fluid mobility in the tuff reservoirs of the Huoshiling Formation from the Dehui Fault Depression, southeastern Songliao Basin. Through physical property analysis, X-ray diffraction (XRD), field emission scanning electron microscopy (FE-SEM), thin section (TS), pressure-controlled porosimetry (PCP), rate-controlled porosimetry (RCP), and nuclear magnetic resonance experiments (NMR) on ten tuff samples, we conducted a comprehensive and in-depth exploration of the influencing factors that control the mobility of reservoir fluids. The results indicate: 1) The primary mineral types in the tuff reservoirs are quartz, feldspar, and clay minerals, with porosity predominantly characterized by dissolution pores and intergranular pores; 2) Based on the morphology of PCP intrusion curves, the tuff samples from the study area can be categorized into three types, with reservoir quality progressively deteriorating from Type I to Type III; 3) Compared to the movable fluids saturation (MFS), movable fluids porosity (MFP) is more suitable for characterizing fluid mobility. The mobility of fluids is influenced by various factors such as mineral composition, physical property, pore-throat connectivity, pore type and heterogeneity. MFS and MFP show a positive correlation with permeability, the content of quartz and feldspar, median pore-throat radius (R_{50}), average throat radius (ATR), average pore-throat radius ratio (APT), T_2 cutoff value ($T_{2\text{-}C}$), average throat radius (R_T), sorting coefficient (SC), and intergranular pore dominate space (Inter-DS), while a negative correlation with the content of calcite and clay minerals, average pore-throat radius ratio, and the fractal dimension from NMR (D_{NMR}). This study elucidates the influencing factors of fluid mobility in tuff reservoirs, which has

important reference significance for the scientific development of this type of gas reservoir.

KEYWORDS

tuff reservoirs, pore-throat structure, fluid mobility, huoshiling formation, Songliao Basin

1 Introduction

Volcanic rock reservoirs represent a critically important type of unconventional hydrocarbon resource, occupying a significant position within the global energy sys-tem (Huang, et al., 2012; Liu, et al., 2021; Schutter, 2003; Tian, et al., 2022). The deep formations in the southern Songliao Basin of China harbor abundant natural gas resources within volcanic rocks (Han, et al., 2024; Jiang, et al., 2017; Shan, et al., 2023). As a successful example of volcanic gas reservoir development in China, the Changling No. 1 gas field targets the Lower Cretaceous Yingcheng Formation, consisting of rhyolite and tuff. Since its large-scale development commenced in 2006, the field has cumulatively produced over 100 × 108 m3 of gas. In recent years, Jilin Oilfield (PetroChina) has shifted exploration and development focus to the southeastern part of the Songliao Basin in the Dehui Fault Depression. The objective is the tuff reservoirs of the Huoshiling Formation, where horizontal wells have been deployed to enhance gas productivity. Significant progress has been made in development, culminating in the establishment of a demonstration base producing 2 × 108 m3 of gas annually. This initiative represents a critical area for future gas reserve enhancement and production increase in Jilin Oilfield. Current research on volcanic rock reservoirs primarily focuses on weathered crust areas, with comparatively less attention given to volcanic sedimentary rock domains (Liu, et al., 2022; Tian, et al., 2019; Zhang, et al., 2022b). Previous studies suggest that favorable reservoir development in volcanic rocks is primarily controlled by sedimentary environment, structure, lithofacies, faults, and source-reservoir connectivity (Liu, et al., 2009; Wang, et al., 2010; Wang, et al., 2012; Huang, et al., 2021; Hu, et al., 2023; Tang, et al., 2023; Yang, et al., 2023). However, these understandings of controlling factors for favorable volcanic rock reservoirs are more applicable to rhyolite reservoirs with developed fractures, rather than tuff reservoirs characterized by low to moderate porosity, tightness, and lack of fractures (Becker, et al., 2019; Yu, et al., 2023). Previous research has predominantly concentrated on macroscopic levels, overlooking the controlling role of reservoir microscopic pore structures on fluid mobility. The microscopic pore structure and its heterogeneity control reservoir fluid flow capacity, determining well productivity, stable production capacity, and recovery rates. Therefore, studying the relationship between reservoir pore structure and fluid mobility is of significant importance in enhancing gas field development (Zhang, et al., 2022a).

Fluid mobility research is crucial for the evaluation of resources and plays a sig-nificant role in the development of oil and gas (Dong, et al., 2023; Pang, et al., 2022; Qiao, et al., 2020a). The content of movable fluids serves as an important reference factor for reservoir evaluation and enhanced oil and gas recovery. Due to the complex pore structures, poor pore-throat connectivity, and pronounced heterogeneity of tight res-ervoirs, fluid mobility differs markedly from that of conventional reservoirs (Qu, et al., 2022). By investigating the relationship between pore throat space and fluid mobility, we can enhance our understanding of fluid flow characteristics in tight reservoirs, which, in turn, aids in the optimization of development plans.

In numerous prior studies, nuclear magnetic resonance (NMR) technology has primarily been employed to characterize fluid mobility (Zhang, et al., 2022a). Specifically, the mobile fluid content is determined by comparing the NMR T2 spectra obtained be-fore and after centrifugation (Gao and Li, 2016). Initially, the T2 cutoff value is determined from the cumulative porosity curves derived from NMR data, obtained prior to and following centrifugation. Following this, the pore throat radius that aligns with the T2 cutoff value is recognized as the crucial radius for differentiating between mobile and bound fluids. The movement of fluids is primarily limited by capillary forces when the pore-throat radius is less than this critical value. Due to variations in pore-throat struc-tures, significant differences in T2 cutoff values can be observed among samples. How-ever, numerous studies have indicated that movable fluids can still exist in spaces smaller than the critical radius. Thus, relying solely on the T2 cutoff value or critical radius is insufficient to completely differentiate movable fluids from bound fluids (Lai, et al., 2018a). This limitation arises from the fact that bound water in larger pores after cen-trifugation is distributed as a water film along the surface of the pore-throat. As a result, scholars have suggested the bound water film model to examine the capacity for fluid flow, with the intention of enhancing the comprehension of fluid movement throughout various pore throat regions (Huangshan, et al., 2018). The attributes of pore size distribu-tion are considered a vital element in assessing the connection between pore structure and fluid mobility. According to Lala and EI Sayed (2017), fluid flow capacity is notably influenced by the presence of micropores and throats (Lala and El-Sayed, 2017).

Xiao's study reveals that fluid flow mechanisms in tight sandstone reservoirs are fundamentally distinct from those in conventional reservoirs, mainly because of differences in the composition of pores (micro and nano scale). (Xiao, et al., 2017). Addi-tionally, Dong's research establishes that pore throat radius of 0.1 μm and 1 μm, respec-tively, influence the fluid mobility and permeability of tight sandstone reservoirs within the Shanxi Formation, Ordos Basin (Dong, et al., 2023). The type and content of minerals significantly affect fluid mobility, a finding corroborated by numerous scholarly stud-ies (Basso, et al., 2022; Ma, et al., 2017; Zang, et al., 2022). It is widely accepted that quartz and feldspar enhance the flow capacity of fluids, whereas carbonate and clay minerals tend to inhibit fluid mobility (Zhang, et al., 2022a). Furthermore, a strong positive corre-lation exists between fluid mobility and reservoir heterogeneity; as reservoir heteroge-neity

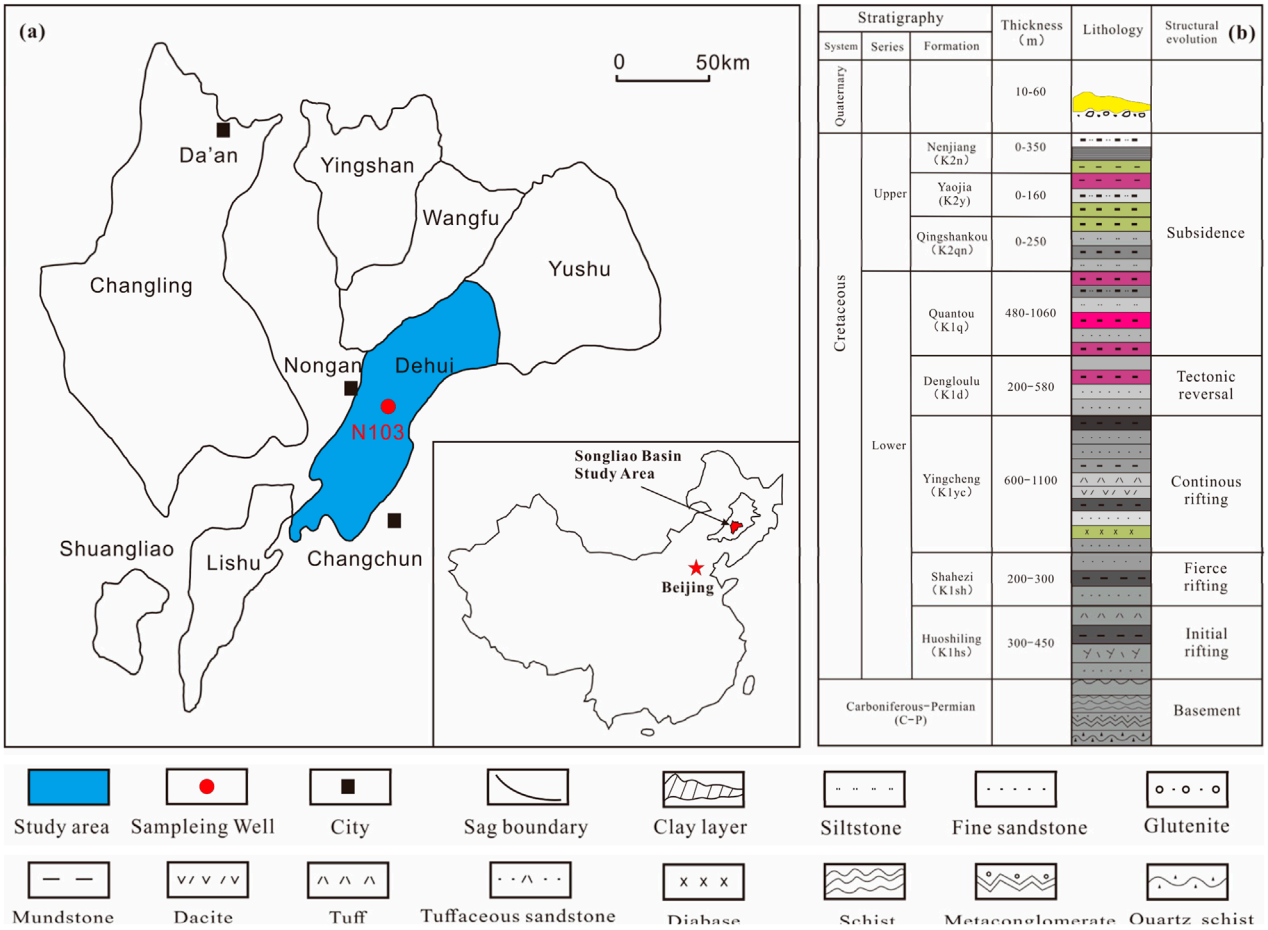

FIGURE 1
Location of the study area and sampling well in Songliao Basin, China **(A)**; comprehensivehistogram of Dehui fault depression stratum **(B)**.

increases, the complexity of the pore structure also rises, resulting in diminished fluid mobility (Wang, et al., 2020a).

This paper integrates physical property analysis, X-ray diffraction (XRD), field emission scanning electron microscopy (FE-SEM), thin section (TS), pressure-controlled porosimetry (PCP), rate-controlled porosimetry (RCP), and nuclear magnetic resonance experiments (NMR) to comprehensively characterize the microscopic pore structures of tuff reservoirs in the Huoshiling Formation, Dehui Sag, southern Songliao Basin. It ex-plores the coupling relationship between fluid mobility and porosity, permeability, mineral composition, pore type, pore-throat connectivity and reservoir heterogeneity. revealing the primary factors controlling fluid mobility. Ultimately, this research aims to guide the efficient development of tuff gas reservoirs in the study area.

2 Geological setting

The study area is located in the southern part of the Songliao Basin, within the eastern fault depression zone of the Dehui Fault Depression (Figure 1). It is bordered to the north by the Wangfu and Yushu Fault Depressions and to the southwest by the Huaiwei Uplift across from the Lishu Fault Depression (Jiang, et al., 2017). The target strata are the third segment of the Huoshiling Formation of the Lower Cretaceous. Structurally, the Dehui Fault Depression is predominantly influenced by north-northeast-oriented faults, creating a "ridge, trench, step" structural pattern. During the Huoshiling Formation period, fissure-style volcanic eruptions produced a set of tuff reservoirs. The subfacies types mainly include volcanic vent facies, near-vent facies, and volcanic sedimentary facies. The lithology of the tuff reservoirs is primarily composed of brecciated tuff, breccia-bearing tuff, and sedimentary tuff, characterized by a lack of sorting, rounding, or oriented arrangement. Porosity is mainly constituted by matrix micropores and dissolution pores, with underdeveloped microfractures. Core analysis indicates that porosity generally ranges between 6% and 15%, with a median of 10.8% and an average of 9.7%. Permeability typically ranges from 0.032 mD to 1.024 mD, with a median of 0.09 mD and an average of 0.16 mD, exhibiting typical characteristics of a medi-um-high porosity, tight reservoir.

3 Samples and methods

A total of ten samples were used in this study, sourced from Well N103, which is located in the central part of the Dehui Sag

10.3389/feart.2024.1502160

TABLE 1 Porosity, permeability and mineralogy.

NO	Sample ID	Depth (m)	Porosity (%)	Permeability (mD)	Quartz (%)	Feldspar (%)	Calcite (%)	Dolomite (%)	Clay (%)
1	N2	2321.21	7.21	0.0023	26.1	23.8	5.3	0.9	43.9
2	N3	2322.28	2.31	0.0027	25.7	24.8	5.3	0.6	43.6
3	N7	2324.03	9.58	0.0081	33.5	36.4	6.6	4.7	18.8
4	N8	2325.18	10.33	0.0063	29.6	33.4	8.8	3.5	24.7
5	N11	2327.14	8.58	0.0055	33.3	21.1	9.2	0.7	35.7
6	N12	2328.44	13.50	0.3837	43.8	47.8	0.5	0.6	7.3
7	N15	2330.86	9.58	0.0095	36.7	39.7	2.7	0.7	20.2
8	N16	2331.46	13.66	0.2372	42.0	36.4	1.3	3.5	16.8
9	N19	2335.58	6.87	0.0278	35.3	32.8	5.5	2.6	23.8
10	N20	2336.55	11.09	0.0365	41.8	43.3	0.5	0.6	13.8

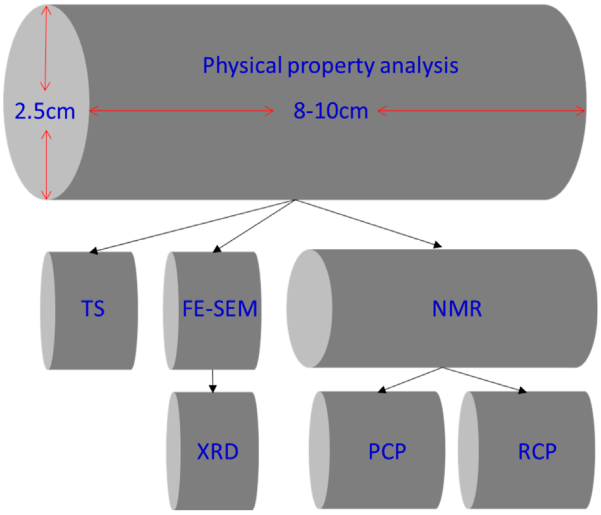

FIGURE 2
Schematic illustration of the experiments.

(Figure 1), at depths ranging from 2321.21m to 2336.55 m (Table 1). The lithology of the samples is grey-green tuff.

Initially, the samples were prepared as core columns with a diameter of 2.5 cm. Before the commencement of experiments, all samples underwent oil washing and drying treatments. The following experimental procedures were sequentially conducted: physical property analysis, XRD, TS, FE-SEM, NMR, PCP and RCP (Figure 2). Before the commencement of experiments, all samples underwent oil washing and drying treatments. After undergoing oil washing and drying treatment, the sample was divided into three segments measuring approximately 2 cm, 2 cm, and 4 cm, which were subsequently subjected to TS, FE-SEM, and NMR experiments, respectively. XRD testing was conducted on the samples that had undergone FE-SEM analysis. Additionally, the NMR tested sample was split into two-halves, and PCP and RCP tests were performed separately on each half.

Prior to the FE-SEM experiments, it is essential to perform mechanical cutting and argon ion profiling on the samples (utilizing the Ilion+II 697C argon ion profiling in-strument). Subsequently, the QUANTA FEG 450 FE-SEM is employed to obtain pore throat information of the samples. NMR experiments were conducted using a MR Cores-XX high-precision benchtop nuclear magnetic resonance core analyzer, with an echo spacing of 70 us, a wait time of 10 s, an echo count of 8000, and 32 scanning repeti-tions. The centrifuge used was a CSC-12 model, with a maximum rotation speed of 12,000 r/min and a maximum centrifugal force of 400 psi. The PCP experiments were performed using a PoreMaster-60 fully automatic porosimeter, with experimental conditions set at a temperature of 23°C, humidity of 35%. The maximum mercury injection pressure of the PCP porosimeter exceeds 200MPa, and the minimum detection radius is less than 4 nm. We used a an ASPE-730 CMI porosimetry to conduct the RCP experiment, which can obtain three capillary pressure curves including total pore-throat, pore, and throat.

All these experimental projects were conducted at the Key Laboratory of Uncon-ventional Oil and Gas Reservoir Formation

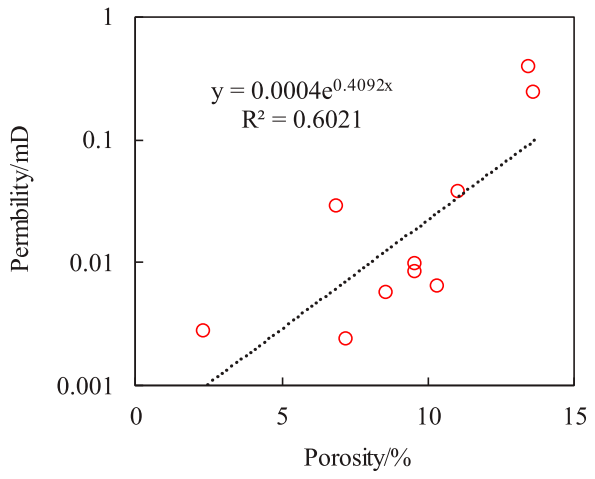

FIGURE 3
Cross-plot of porosity and permeability.

and Development of Heilongjiang Province at Northeast Petroleum University.

4 Results

4.1 Petrophysical properties and mineralogy

The results of porosity, permeability, and mineral content measurements are shown in Table 1. There is considerable variation in the physical properties of different samples, with porosities ranging from 2.31% to 13.66% and an average of 9.27%. Permeability ranges from 0.0023 mD to 0.3837 mD, with an average of 0.072 mD, consistent with the standards of a typical tight reservoir. A scatter plot of porosity and permeability reveals a positive correlation, indicating a general trend of increasing permeability with porosity (Figure 3). However, the correlation coefficient R^2 is only 0.602. For some samples with similar porosities, there are orders of magnitude differences in their corresponding permeabilities, suggesting the presence of "ineffective porosity" in these samples, where certain pores do not contribute to reservoir permeability. The mineral composition of the tuff samples predominantly includes quartz, feldspar, and clay minerals, with average contents of 34.8%, 34.0%, and 24.9%, respectively. Additionally, there are significant amounts of calcite and minor dolomite, with average contents of 4.6% and 1.8%, respectively.

4.2 Pore types

Observations from TS and FE-SEM images show that the tuff samples of the study area mainly develop dissolution pores and intergranular pores, with occasional microfractures (Figures 4A–C). Dissolution pores are the most developed and can be subdivided into two types: matrix dissolution pores (Figure 4A) and mineral dissolution pores (Figures 4B, D). Matrix dissolution pores primarily result from the dissolution of volcanic ash under acidic fluid action, are relatively small in size, often less than a few micrometers, and exhibit a honeycomb-like contiguous distribution with good connectivity. Mineral dissolution pores are mainly found within feldspar minerals, are sporadically distributed, with pore sizes ranging from a few to several tens of micrometers, and are isolated with poor connectivity. Intergranular pores primarily originate from clay minerals, predominantly illite, illite-smectite mixed layers, and chlorite, and are mostly nanometer-sized pores with poor connectivity (Figures 4E, F). Microfractures are relatively undeveloped in the study area, with occasional dissolution fractures, which are important pathways for enhancing reservoir permeability (Figure 4C).

4.3 PCP

Based on the morphology of the PCP intrusion curves, the tuff samples can be classified into three categories (Figure 5A), with pore structure quality progressively deteriorating from Type I to Type III (Table 2). For Type I samples, typified by sample N16, exhibit the lowest displacement pressure at only 0.48 MPa. The mercury intrusion curve displays a gently sloping ramp, indicating good pore-throat connectivity. At an injection pressure of 10 MPa, mercury intrusion exceeds 50% (Figures 5A–1), with maximum mercury saturation greater than 90%. The porethroat radius distribution curve shows a typical bimodal distribution, with peaks at 35 nm and 350 nm respectively (Figures 5B–1). For Type II samples, exemplified by sample N15, have an increased dis-placement pressure of 0.72 MPa. Below 10 MPa injection pressure, the mercury intrusion curve exhibits a distinct slope, corresponding to a mercury saturation of less than 20% (Figures 5A–2). The maximum mercury saturation reaches 81.89%, with the pore-throat radius distribution curve displaying a unimodal distribution, peaking at 40 nm (Figures 5B–2). For Type III samples, represented by sample N2, have a higher displacement pressure of 2.61 MPa. The mercury intrusion curve lacks a flat segment, with maximum mercury saturation below 60% (Figures 5A–3). The pore-throat radius distribution curve also presents a unimodal distribution, peaking at 10 nm (Figures 5B–3), indicating poorly developed porosity.

4.4 RCP

The maximum mercury injection pressure in the RCP experiment is 6.2 MPa, which, ac-cording to the Washburn equation, allows for the characterization of a minimum pore size of 0.12 μm (Xiao, et al., 2016; Zhang, et al., 2017). As illustrated in Figure 5, the analysis of the morphology of the RCP capillary pressure curves categorizes the tuff samples into three distinct types, con-sistent with the results of the PCP experiments. The Type I sample is pore-dominated (Figure 6A, Sample N16), where the shape of the total mercury injection curve is primarily influenced by the pore mercury injection curve. At lower mercury injection pressures (<1 MPa), pore mercury in-jection predominates; however, at higher pressures, throat mercury injection becomes dominant. The final accumulated mercury saturation for this type is approximately 70%, indicating a well-developed pore structure with good connectivity. The Type II

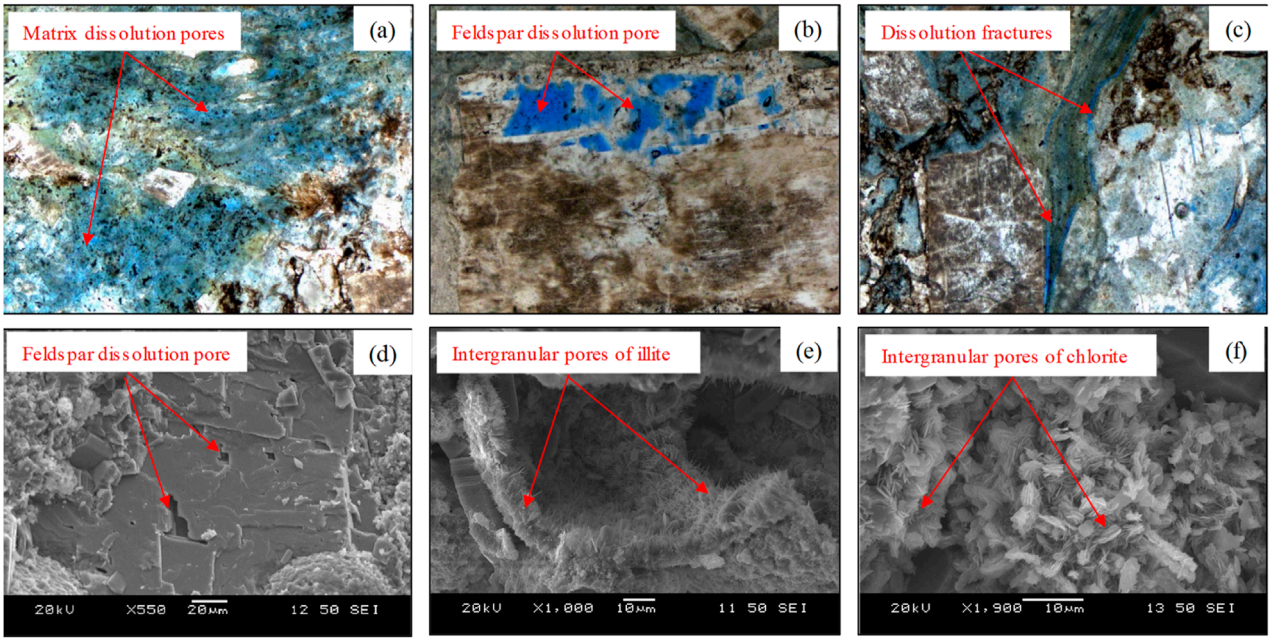

FIGURE 4
Pore types of the tuff samples. **(A)** Matrix diss olution pores, **(B)** Feldspar dissolution pore, **(C)** Diss olution fractures, **(D)** Feldspar dissolution pore, **(E)** Intergranular pores of illite, **(F)** Intergmnular pores of chlorite.

sample is classified as pore-throat co-dominant (Figure 6B, Sample N15), in which the total mercury injection is gov-erned by both pore and throat mercury injections. Under lower pressure conditions, mercury is uniformly injected into both pores and throats. As the pressure reaches 1 MPa, throat mercury injection becomes the predominant mechanism, resulting in a final mercury saturation of 53.06%. The Type III sample is throat-dominated (Figure 6C, Sample N2), where the total mercury injection is primarily controlled by throat mercury injection. These samples exhibit underdeveloped pores and poor connectivity, yielding a total mercury saturation of only 37.51%.

The pore radius distribution curves exhibit no significant differences, with measurements ranging from 100 to 300 μm and a peak around 120 μm (Figure 7A). In contrast, the throat radius distribution curves show significant differences (Figure 7B). As the classification level increases, the throat radius distribution curve progressively shifts to the right, with peak values of 0.3 μm, 0.7 μm, and 1.0 μm, respectively. Conversely, the characteristics of the pore-throat radius ratio distribution curve are opposite to those of the throat radius distribution curve. As the classification level increases, the pore-throat radius ratio distribution curve shifts gradually to the left, with peak values of 75, 180, and 360, respectively (Figure 7C).

The RCP injection curve not only distinguishes between pores and throats but also classifies pore types based on the shape of the mercury injection curve within the pores (Qu, et al., 2020; Xiao, et al., 2018). Xiao's research indicates that the reservoir space of tight sandstone can be categorized into intergranular poredominated and intragranular poredominated spaces, each corresponding to different pore connectivity relationships (Xiao, et al., 2018). For example, sample N16, as illustrated in Figure 8, features a horizontal straight line drawn at the inflection point of the pore mercuryinjection curve, which divides the reservoir space into intergranular pore-dominated and intragranular pore-dominated areas. Notably, the percentage of intergranular pore-dominated space accounts for 79.8% of the total pores. As detailed in Table 3, the proportion of intergranular poredominated space in ten tuff samples ranges from 33.0% to 79.8%, with an average of 53.7%.

4.5 Nuclear magnetic resonance experiment

4.5.1 Characteristics of T_2 spectrum curves

Nuclear magnetic resonance (NMR) technology offers non-destructive and rapid characterization of reservoir pore structures, and its importance has been increasingly recognized in recent years (Singh, et al., 2022; Zhang, et al., 2019). Figure 8 show the typical NMR T2 spectra for the samples, which, similar to the capillary pressure curves from PCP, display distinctly different features among the three types of tuff samples. Sample N16's T2 spectrum exhibits a bimodal structure, with the right peak quite larger than the left, where the left and right T2 peaks are respectively 2 ms and 25 ms (Figure 9A). Sample N15's T2 spectrum also develops a bimodal structure but with the left peak greater than the right, where the left and right T2 peaks are respectively 5 ms and 100 ms (Figure 9B). Sample N2's T2 spectrum shows a unimodal structure with a peak value of 0.6 ms (Figure 9C).

4.5.2 Characteristics of T_2 spectrum curves

Based on a comparison of the T2 spectrum curves before and after centrifugation, the bound water model can be employed

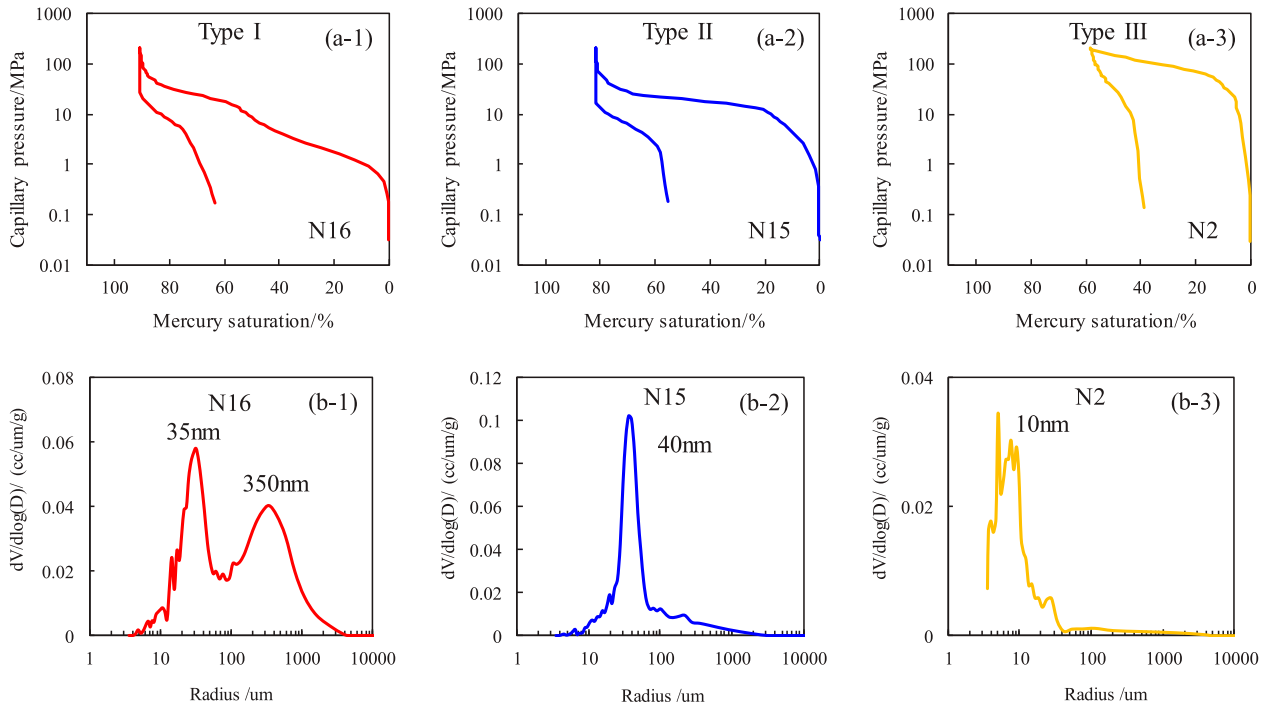

FIGURE 5
Pressure-controlled porosimetry curves **(a-1,a-2,a-3)**, and pore size distribution curves **(b-1,b-2,b-3)** for three types of samples.

TABLE 2 Parameters of PCP and types of the tuff samples.

NO.	Sample ID	P_d (MPa)	R_m (um)	P_{50} (MPa)	R_{50} (um)	SC	Type
1	N2	2.61	0.28	89.83	0.0082	0.41	III
2	N3	1.46	0.50	111.35	0.0066	0.38	III
3	N7	1.43	0.51	36.40	0.0202	0.43	III
4	N8	2.40	0.30	39.12	0.0188	0.47	III
5	N11	1.91	0.38	46.33	0.0159	0.35	III
6	N12	0.28	2.58	7.97	0.0922	0.70	I
7	N15	0.72	1.01	17.98	0.0409	0.37	II
8	N16	0.48	1.51	6.05	0.1215	0.61	I
9	N19	0.90	0.81	14.75	0.0798	0.55	II
10	N20	0.31	2.33	14.97	0.0491	0.58	II

Note: P_d-threshold pressure; R_m-maximum pore-throat radius; P_{50}- median pressure; R_{50}-median radius; SC: sorting coefficient.

to determine mobile fluid saturation (MFS), which indicates the percentage of connected pore volume relative to the total pore volume. The product of MFS and porosity is referred to as movable fluid porosity (MFP), representing the content of the space that influences fluid flow (Dong, et al., 2023). Sta-tistical results (Table 3) reveal that the Type I samples exhibits high content of movable fluid, with average values of 39.88% and 5.41% for MFS and MFP, respectively. In con-trast, the movable fluid space in the type II samples are relatively reduced, showing average values of 32.61% for MFS and 2.95% for MFP. The NMR T2 spectra of the Type III samples before and after centrifugation nearly overlap, indicating a further reduc-tion in movable fluid space, with average values of

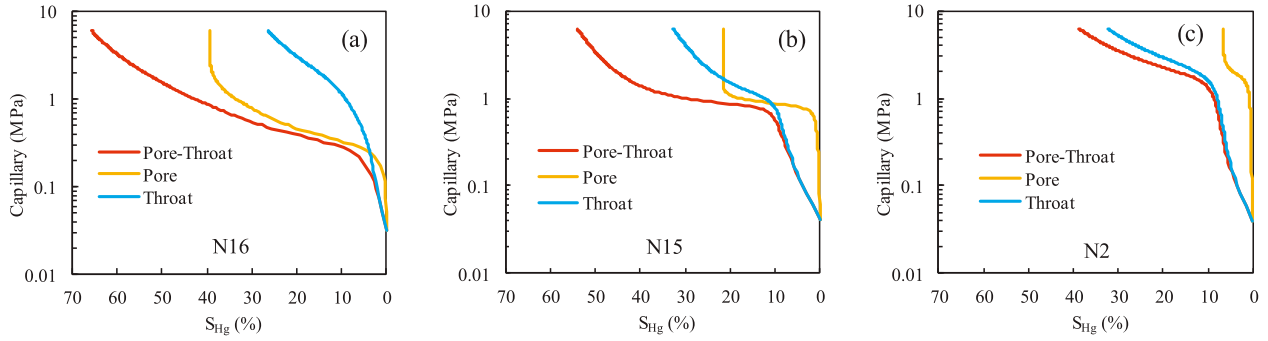

FIGURE 6
Rate-controlled porosimetry curves for three types of samples. **(A)** Type I, **(B)** Type II, **(C)** Type III.

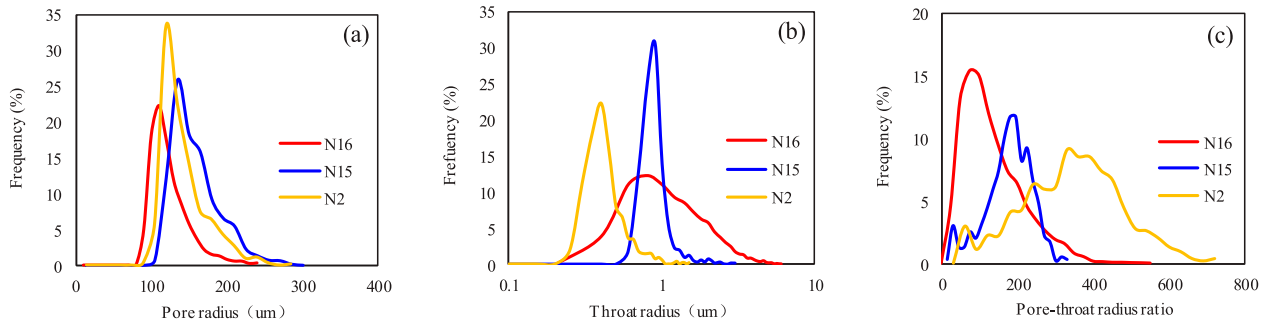

FIGURE 7
Pore radius, throat radius, and pore-throat radius ratio curves for three types of samples. **(A)** Type I, **(B)** Type II, **(C)** Type III.

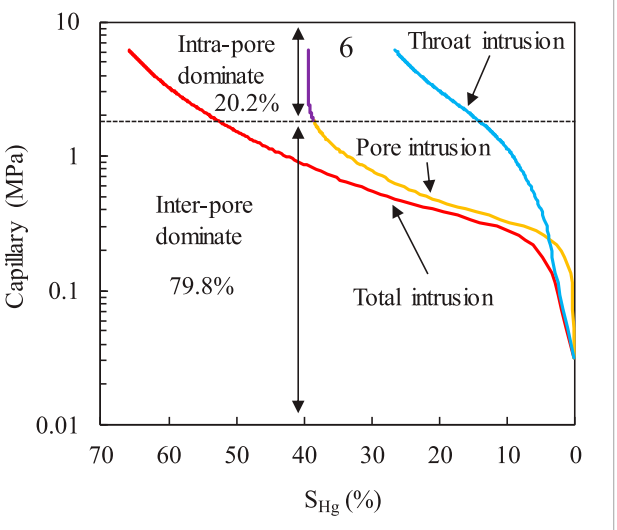

FIGURE 8
Contributions of intragranular and intergranular pore dominate space to the total reservoir space of Sample N16.

18.16% for MFS and 1.50% for MFP. Notably, there are significant differences in the occurrence state of movable fluids among the three types of samples, which will directly impact the flow of gases within the reservoir.

4.5.3 Fractal dimension

Fractal theory is an effective tool for characterizing the microscale heterogeneity of reservoir pore structures and has been widely applied in tight sandstones, shales, coals, and other reservoirs since its introduction (Li, et al., 2022; Zhang, et al., 2024; Zhang, et al., 2020; Zhang, et al., 2021). Based on data from high-pressure mercury intrusion experiments, low-temperature nitrogen adsorption experiments, and nuclear magnetic resonance experiments, scholars have proposed various mathematical models to calculate fractal dimensions. To more comprehensively characterize the heterogeneity of the pore structures in the tuff reservoirs of the study area, this research employs NMR data to calculate the fractal dimensions. Assuming the reservoir's microscopic pore system is spherical, the nuclear magnetic resonance fractal dimension calculation model can be represented as follows (Li, et al., 2022; Pang, et al., 2022):

$$\log\left(\sum_{j}^{n}\frac{V_{pi}}{T_{2j}^{3}}\right) = -\mathrm{Dflog}(T_{2i}) - \mathrm{Dflog}(3\rho) - \log\left(36\pi\rho^{3}\right) \quad (1)$$

Where V_{pi} corresponds directly to T2i, j = i + 1, ρ represents the conversion coefficient associated with each T_2 value.

TABLE 3 Parameters of PCP and NMR.

NO.	Sample ID	APR (μm)	ATR (μm)	APT	P_{Inter} (%)	$T_{2\text{-}C}$ (ms)	MFS (%)	MFP (%)	D_{NMR}
1	N2	139.74	0.23	604	33.0	0.58	13.74	0.99	2.9376
2	N3	147.34	0.20	726	36.6	0.97	10.45	0.24	2.9738
3	N7	155.73	0.41	380	41.3	1.37	24.74	2.37	2.8347
4	N8	161.51	0.45	360	45.1	3.03	17.79	1.84	2.8829
5	N11	141.00	0.37	381	49.3	2.39	24.08	2.07	2.9016
6	N12	163.64	0.81	202	79.8	12.91	43.96	5.94	2.5795
7	N15	157.00	0.55	285	58.2	5.17	33.62	3.22	2.7768
8	N16	157.84	0.72	219	75.8	11.16	35.79	4.89	2.6039
9	N19	158.49	0.47	336	49.3	7.59	35.33	2.43	2.6775
10	N20	152.00	0.62	244	68.1	9.38	28.87	3.20	2.7658

Note: APR-average pore radius; ATR-average throat radius; APT-average pore-throat radius ratio; P_{Inter}-percentage of intergranular pore dominate space; $T_{2\text{-}C}$- T_2 cutoff value; MFS-movable fluid saturation; MFP-movable fluid porosity; D_{NMR}-fractal dimension based on NMR.

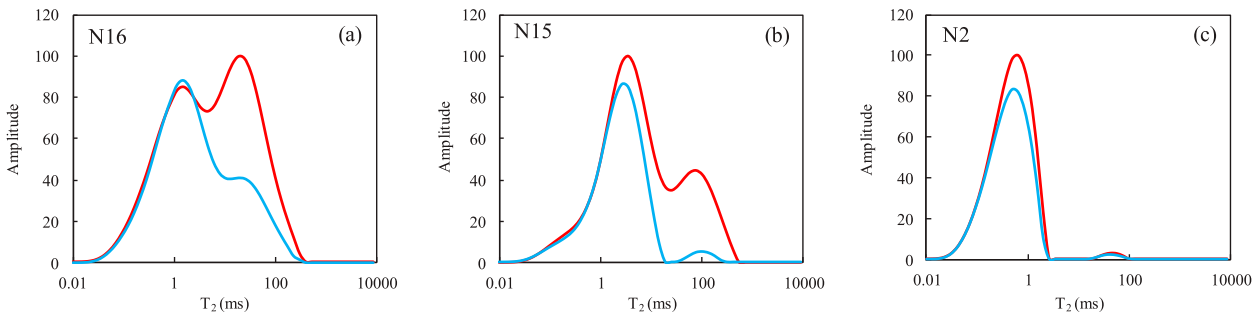

FIGURE 9
T_2 spectrum distribution curves for three types of samples. **(A)** Type I, **(B)** Type II, **(C)** Type III.

Equation 1 can be further simplified as follows:

$$y = kx + b$$

Where k represents the slope of the fitted line, which is the calculated fractal dimension.

The fractal dimension serves as a pivotal metric for evaluating the relationship between microscopic pore structures and macroscopic physical properties (Dou, et al., 2021). Theoretically, fractal dimensions typically range between 2 and 3. A higher fractal dimension (approaching 3) indicates a more complex pore structure, whereas a lower value (approaching 2) suggests a simpler structure (Mandelbrot, 1975; Mandelbrot 1982; Yao, et al., 2008). The fractal dimensions are calculated using the NMR T_2 spectra data of the samples in their saturated state. As shown in Figure 10, the Log (N (rj))-Log (T_2) curves of three typical samples exhibit strong positive correlations, with correla-tion coefficients of 0.9837, 0.9696, and 0.9768 respectively. These high values indicate that the pore structures within the tuff reservoirs of the study area exhibit fractal characteristics.

The fractal dimensions of the tuff reservoir samples in the study area range from 2.5795 to 2.9738, with an average of 2.7933 (Table 2). Among these, Type I samples dis-play the least heterogeneity, with sample N16 having a DNMR of 2.6039. Type II samples exhibit moderate heterogeneity, with sample N15's DNMR calculated at 2.7768; and Type III samples show the strongest heterogeneity, with sample N15's DNMR reaching 2.9376. This gradient in fractal dimensions across the sample types further illustrates the increasing complexity and heterogeneity in pore structure from type I through type III.

5 Discussion

5.1 Impact of petrophysical properties and mineral content on fluid mobility

The relationship between fluid mobility parameters and porosity, permeability is illustrated in Figure 11. Both MFS and MFP exhibit

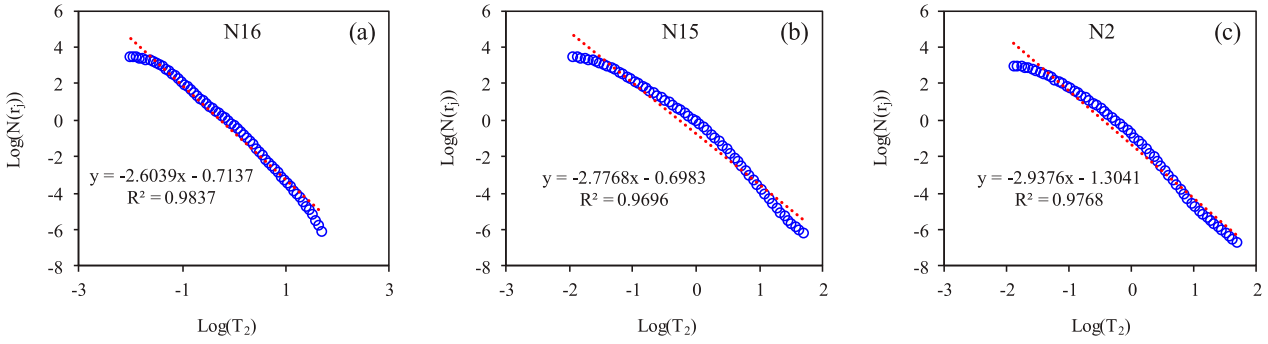

FIGURE 10
Fractal characteristics for three types of samples. **(A)** Type I, **(B)** Type II, **(C)** Type III.

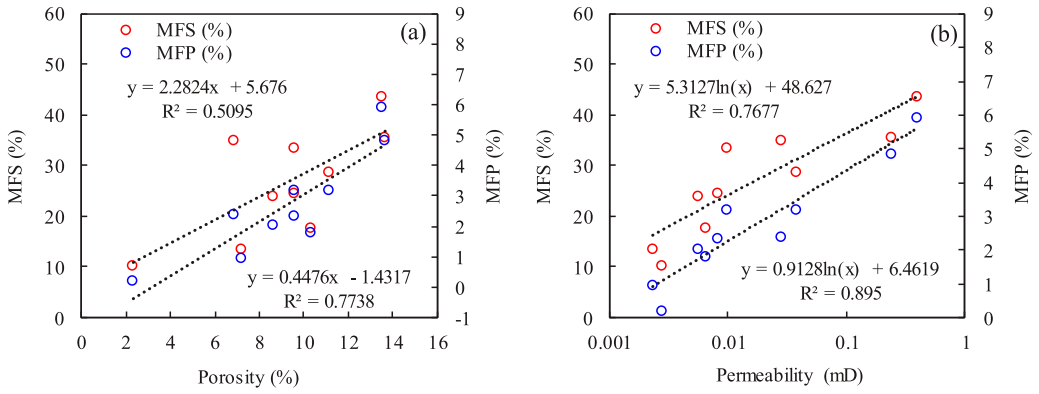

FIGURE 11
Relationships between porosity **(A)**, permeability **(B)** and fluid mobility parameters.

a positive correlation with porosity (R^2 = 0.5095, R^2 = 0.7738, respectively). However, the positive correlation between MFS and MFP with permeability is significantly stronger than that with porosity (R^2 = 0.7677, R^2 = 0.8950). This suggests that permeability is the primary factor influencing fluid mobility, enhanced reservoir connectivity corresponds to increased fluid mobility, which aligns with the findings of Dong et al. (2023). Notably, MFP demonstrates a higher correlation with permeability compared to MFS, indicating that MFP is more effective for evaluating reservoir quality.

Pore type, pore size, pore geometry, connectivity of pore system and textural properties are the result of a combination of sedimentary and diagenetic alterations, and mineralogy provides quantitative traces and consequences of these effects (McKinley et al., 2011). In examining the relationship between mineral content and fluid mobility pa-rameters within tuff reservoirs, a detailed correlation analysis involving quartz, feldspar, calcite, and clay minerals was conducted (Figure 12). The results highlighted a positive correlation between quartz and feldspar contents with MFS and MFP (Figures 12A, B), attributed to quartz's resistance to deformation and compaction and feldspar's susceptibility to dissolution in acidic environments, which enhances porosity and connectivity (Qiao, et al., 2020a; Qiao, et al., 2020b). Conversely, MFS and MFP negatively correlated with calcite and clay (Figures 12C, D). Calcite, while potentially creating porosity through dissolution, predominantly acts as a cementing agent when abundant, obstructing pore throats and reducing fluid mobility. Similarly, clay minerals, products of feldspar dis-solution, tend to clog pores and decrease fluid mobility (Wang, et al., 2020b).

5.2 Impact of pore-throat connectivity on fluid mobility

Many publications have suggested that the pore-throat connectivity are the intrin-sic controlling factors for the fluid mobility. Pore structure, encompassing pore and throat sizes, geometrical shapes, pore size distribution, and connectivity, fundamentally governs the storage and flow capacity of reservoirs at the microscopic scale, making it a crucial parameter for reservoir evaluation (Lai, et al., 2018c). As illustrated in Figure 13A, both MFS and MFP show positive correlations with the median radius (R50), with R^2 = 0.7181 and R^2 = 0.7935, respectively. This indicates that pore-throat size predominantly controls the fluid mobility in the tuff reservoirs of the study area.

The fluid mobility parameters (MFS and MFP) exhibit a positive correlation with the average pore radius (Figure 13B). However, this correlation is quite weak, as evidenced by R^2 values of 0.4180 and

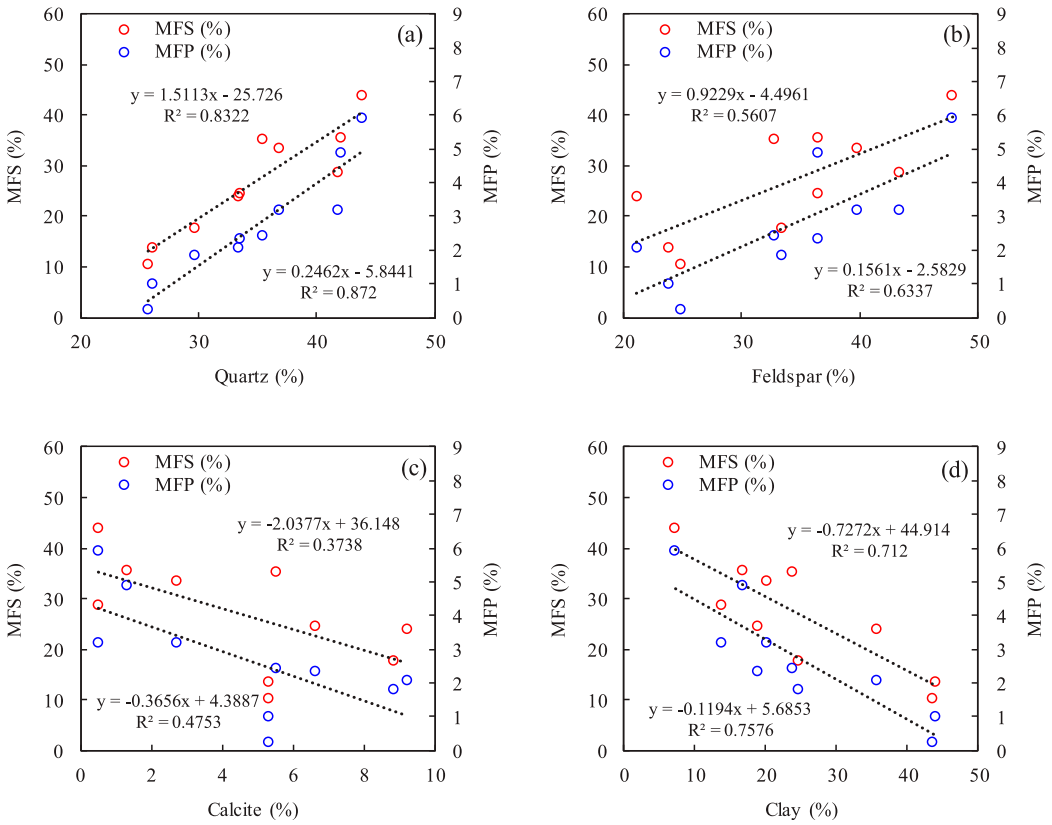

FIGURE 12
Relationships between quartz **(A)**, feldspar **(B)**, calcite **(C)**, clay **(D)** content and fluid mobility parameters.

0.4096, respectively. In contrast, the correlation between MFS and MFP with the average throat radius shows a significant improvement (Figure 13C), with R^2 values of 0.8087 and 0.9158, respectively, as well as with the average pore throat ratio (Figure 13D, R^2 = 0.8087, 0.9158, respectively). These findings indicate that the throat radius, rather than the pore radius, has a more substantial impact on fluid mobility. Similarly, Wang et al. conducted a comprehensive study on the relationship between pore structure and reservoir properties of Triassic tight sandstone oil reservoirs in the Ordos Basin, confirming that throat radius, as opposed to pore radius, significantly influences permeability (Wang, et al., 2020a).

The T_2 cutoff is commonly employed to establish the lower limit of pore radius for movable fluids. In the NMR T_2 spectrum, the fluid in the pores to the right of the T_2 cutoff is regarded as movable, whereas the fluid in the pores to the left is classified as bound (Dong, et al., 2023; Qiao, et al., 2020a). However, some scholars argue that utilizing the T_2 cutoff to differentiate between movable and bound fluids is inappropriate, they contend that the boundary between the movable and irreducible water should be viewed as a range rather than a default value (Huangshan, et al., 2018; Lai, et al., 2018a). As illustrated in Figure 14, both MFS and MFP exhibit a strong positive correlation with $T_{2\text{-}C}$, (R^2 = 0.7593, R^2 = 0.8166, respectively) suggesting that fluid mobility increases as $T_{2\text{-}C}$ rises. This finding indicates that the fluid mobility of the tuff samples in the study area is significantly influenced by the $T_{2\text{-}C}$, which can be utilized to classify fluids as movable or irreducible.

5.3 Impact of intergranular pore dominate space on fluid mobility

The controls of PSDs on the reservoir quality have been thoroughly investigated (Wu, et al., 2017; Xiao, et al., 2017), while the impacts of other parameters such as pore type is rarely involved. As shown in Figure 15, MFS and MFP progressively increase with the rising percentage of intergranular pore dominate space (P_{inter}), indicating that samples exhibiting high fluid mobility possess a larger dominate space for intergranular pores. Consequently, it can be concluded that the intergranular pores significantly influences fluid mobility, whereas the intragranular pores has a relatively minor effect on fluid mobility, despite the good connectivity of the clay mineral pores that primarily constitute intragranular pores. Similarly, Wu et al.'s study found that oil injection predominantly occurs in large pore-throat systems characterized by intergranular pores, thereby indirectly demonstrating the significance of intergranular pores in facilitating fluid mobility. (Wu, et al., 2016).

5.4 Impact of intergranular pore dominate space on fluid mobility

Heterogeneity of pore structure refers to the degree of concentration of pore-throat size distribution (Meng, et al., 2021). To further investigate the impact of reservoir het-erogeneity on the

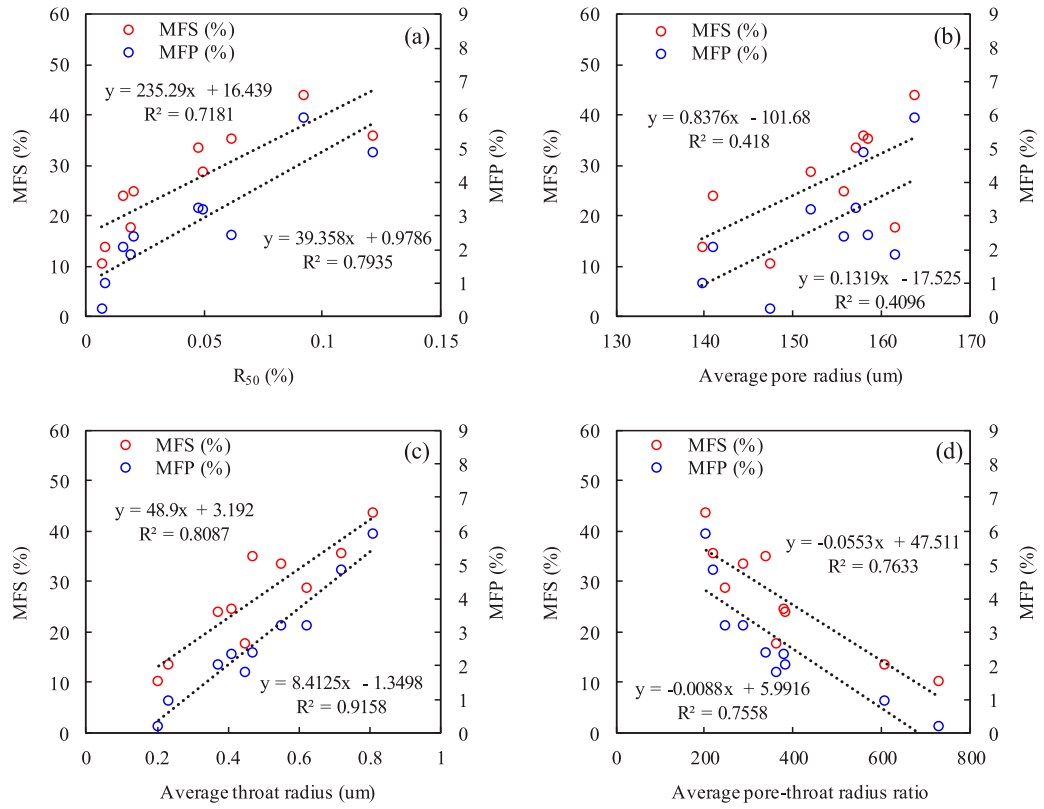

FIGURE 13
Relationships between R50 **(A)**, average pore radius **(B)**, average throat radius **(C)**, average pore-throat radius ratio **(D)** and fluid mobility parameters.

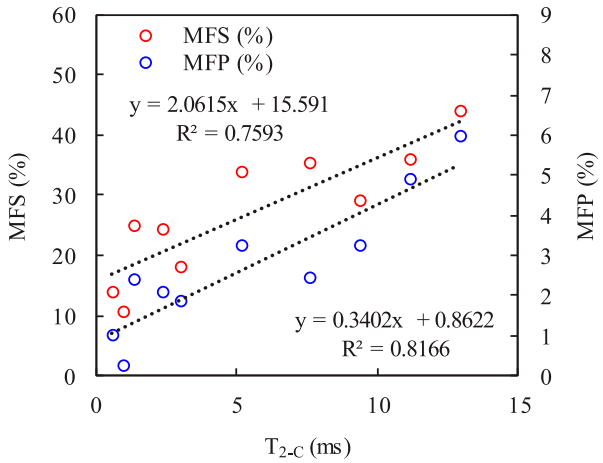

FIGURE 14
Relationships between $T_{2\text{-}C}$ and fluid mobility parameters.

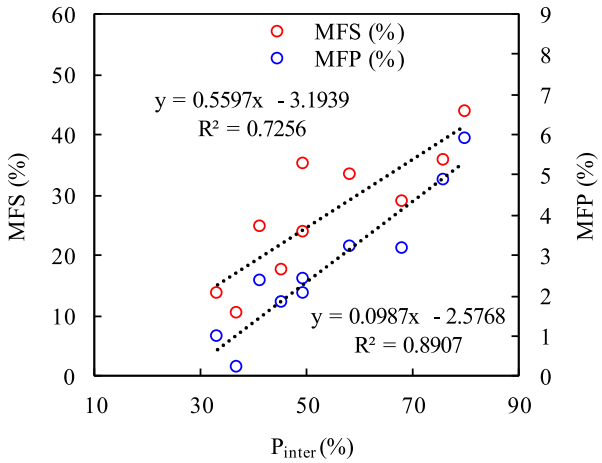

FIGURE 15
Relationships between Pinter and fluid mobility parameters.

permeability of the Huoshiling Formation tuff reservoirs in the study area, the relationships between the sorting coefficient (SC), nuclear magnetic resonance fractal dimension (DNMR), and fluid mobility were examined.

The sorting coefficient, derived from high-pressure mercury intrusion experiments, is used to describe the heterogeneity of pore throat distributions within reservoirs. Typically ranging from 0 to 1, a lower sorting coefficient indicates a more concentrated distribution of pore throat sizes and stronger heterogeneity, while a value closer to one suggests a more uniform distribution (Dong, et al., 2023; Meng, et al., 2021;

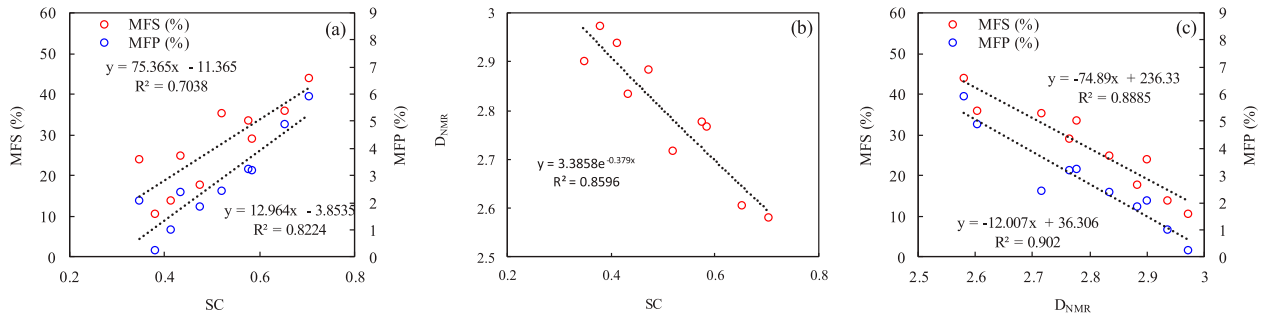

FIGURE 16
Relationship between SC and fluid mobility parameters **(A)**, Relationship between SC adn D_{NMR} **(B)**, Relationship between D_{NMR} and fluid mobility parameters **(C)**.

Zhang, et al., 2022a). Qu et al.'s research indicates that a smaller sorting coefficient corresponds to a more concentrated distribution range of pore-throat size, poorer homogeneity of the reservoir's pore structure, and diminished seepage capacity (Qu, et al., 2020). The sorting coefficients for the tuff reservoir samples in the study area range from 0.35 to 0.70, with an average of 0.49, indicating significant heterogeneity. There is a positive correlation between MFS, MFP and SC, with R^2 of 0.6758 and 7663, respectively Figure 16A. This demonstrates that the microscale heterogeneity of pore structure significantly impacts the fluid flow capacity of the tuff reservoirs.

Many scholars utilize fractal dimension to characterize the heterogeneity of reservoir pore structures (Dou, et al., 2021; Guan, et al., 2020). This is primarily because the dimension not only describes pore structure heterogeneity at the microscopic level but also serves as a bridging parameter for both reservoir micropore structures and macroscopic physical property parameters (Lai, et al., 2018b; Zhang, et al., 2024). The primary advantage of NMR experiments lies in their ability to effectively characterize pore structure characteristics across a range from the nanometer to the micron level. Consequently, the fractal dimension derived from NMR experimental (D_{NMR}) can provide a more comprehensive description of the heterogeneity within the reservoir pore structure (Pang, et al., 2022). The correlation analysis between the D_{NMR} and the SC reveals a strong negative correlation (R^2 = 0.8596, Figure 16B). Specifically, as the SC increases and approaches 1, the homogeneity of reservoir pore systems increases, leading to a gradual weakening of heterogeneity, which in turn results in a decrease in the DNMR. This suggests that the DNMR can serve as a useful parameter for evaluating the heterogeneity of reservoir pore structures.

As shown in Figure 16C, there is a notable negative correlation between fluid mobility parameters and DNMR, with R^2 of 0.8813 and 0.9015, respectively. As the D_{NMR} increases, the heterogeneity of the reservoir also increases, resulting in deteriorating connectivity and ultimately leading to a decrease in fluid mobility. This finding underscores that the flow capacity of tuff reservoirs is primarily controlled by their heterogeneity.

6 Conclusion

(1) The primary mineral types in the study area's tuff reservoirs are quartz, feldspar, and clay minerals, with average contents of 34.8%, 34.0%, and 24.9%, respectively. The porosity is predominantly characterized by dissolution pores and intergranular pores, with occasional microfractures.

(2) Based on PCP and NMR experiments, the tuff samples can be categorized into three Types, with reservoir quality and fluid mobility progressively decreasing from Type I to Type III.

(3) Fluid mobility is influenced by multiple factors, including mineral composition, porosity and permeability, pore-throat connectivity, pore type and reservoir heterogeneity. A higher content of quartz and feldspar minerals enhances the physical properties of the reservoir. This improvement leads to better pore connectivity and an increased proportion of intergranular pores, which control the available space. Consequently, these factors contribute to greater reservoir homogeneity and enhanced fluid mobility.

Data availability statement

The raw data supporting the conclusions of this article will be made available by the authors, without undue reservation.

Author contributions

TL: Writing–original draft, Conceptualization. WZ: Data curation, Writing–review and editing. CC: Software, Writing–review and editing. HS: Resources, Writing–review and editing. WS: Data curation, Formal analysis, Writing–review and editing. PS: Visualization, Writing–review and editing.

Funding

The author(s) declare that financial support was received for the research, authorship, and/or publication of this article. The

authors thank the support from the Science and Technology Special Projects of PetroChina (No. 2023ZZ21), and the Open Fund of Key Laboratory of Exploration Technologies for Oil and Gas Resources (Yangtze University), Ministry of Education (No. K202307).

Conflict of interest

Author TL was employed by PetroChina Usmile Company Limited. Author WZ was employed by China National Logging Corporation. Author WS was employed by Henan Fifth Geological Exploration Institute Co., Ltd.

The remaining authors declare that the research was conducted in the absence of any commercial or financial relationships that could be construed as a potential conflict of interest.

Generative AI statement

The author(s) declare that no Generative AI was used in the creation of this manuscript.

Publisher's note

All claims expressed in this article are solely those of the authors and do not necessarily represent those of their affiliated organizations, or those of the publisher, the editors and the reviewers. Any product that may be evaluated in this article, or claim that may be made by its manufacturer, is not guaranteed or endorsed by the publisher.

References

Basso, M., Souza, J., Hon´orio, B., Melani, L. H., Chinelatto, G. F., Belila, A. M. P., et al. (2022). Acoustic image log facies and well log petrophysical evaluation of the Barra Velha Formation carbonate reservoir from the Santos Basin, offshore Brazil. *Carbonates Evaporites* 37, 50. doi:10.1007/s13146-022-00791-4

Becker, M., Lima, E. F., Waichel, B. L., and Mantovani, I. F. (2019). Pore system quantification and characterization in volcanic rocks: a case study from the Lower Cretaceous Serra Geral group, Parana Basin, Southern Brazil. *J. Pet. Geol.* 42 (3), 301–317. doi:10.1111/jpg.12735

Dong, X., Meng, X., and Pu, R. (2023). Impacts of mineralogy and pore throat structure on the movable fluid of tight sandstone gas reservoirs in coal measure strata: a case study of the Shanxi formation along the southeastern margin of the Ordos Basin. *J. Petroleum Sci. Eng.* 220, 111257. doi:10.1016/j.petrol.2022.111257

Dou, W., Liu, L., Jia, L., Xu, Z., Wang, M., and Du, C. (2021). Pore structure, fractal characteristics and permeability prediction of tight sandstones: a case study from Yanchang Formation, Ordos Basin, China. *Mar. Petroleum Geol.* 123, 104737. doi:10.1016/j.marpetgeo.2020.104737

Gao, H., and Li, H. (2016). Pore structure characterization, permeability evaluation and enhanced gas recovery techniques of tight gas sandstones. *J. Nat. Gas. Sci. Eng.* 28, 536–547. doi:10.1016/j.jngse.2015.12.018

Guan, M., Liu, X., Jin, Z., and Lai, J. (2020). The heterogeneity of pore structure in lacustrine shales: insights from multifractal analysis using N2 adsorption and mercury intrusion. *Mar. Petroleum Geol.* 114, 104150. doi:10.1016/j.marpetgeo.2019.104150

Han, S., Xiang, C., Du, X., Xie, L. F., Huang, J., and Wang, C. S. (2024). Geochemistry and origins of hydrogen-containing natural gases in deep Songliao Basin, China: insights from continental scientific drilling. *Petroleum Sci.* 21, 741–751. doi:10.1016/j.petsci.2023.10.031

Hu, C., Deng, Q., Lin, L., Hu, M., Hou, X., Zong, L., et al. (2023). Lower Cretaceous volcanic-sedimentary successions of the continental rift basin in the Songliao Basin, northeast China: implication in high-quality reservoir prediction and hydrocarbon potential. *Mar. Petroleum Geol.* 158, 106540. doi:10.1016/j.marpetgeo.2023.106540

Huang, F., Zhang, Z., Xu, J., Li, X., Zeng, Y., Xu, R., et al. (2021). Lithospheric extension in response to subduction of the paleo-pacific plate: insights from early jurassic intraplate volcanic rocks in the Sk2 borehole, Songliao Basin, NE China. *Lithos* 380-381, 105871. doi:10.1016/j.lithos.2020.105871

Huang, Z., Liu, B., and Luo, Q. (2012). Main controlling factors and models of Carboniferous volcanic hydrocarbon accumulation in the Malang Sag, Santanghu Basin. *Acta Geol. Sin.* 86, 1210–1216.

Huangshan, H., Sun, W., Ji, W., Zhang, R., Du, K., Zhang, S., et al. (2018). Effects of pore-throat structure on gas permeability in the tight sandstone reservoirs of the Upper Triassic Yanchang formation in the Western Ordos Basin, China. *J. Petroleum Sci. Eng.* 162, 602–616. doi:10.1016/j.petrol.2017.10.076

Jiang, F., Cheng, R., Ruan, B., Lin, B., Xu, Z., and Li, Z. (2017). Formation mechanism of volcanic reservoirs within a volcanostratigraphic framework: the case of the Wangfu fault depression in the Songliao Basin, China. *Mar. Petroleum Geol.* 84, 160–178. doi:10.1016/j.marpetgeo.2017.03.036

Lai, J., Wang, G., Cao, J., Xiao, C., Wang, S., Pang, X., et al. (2018a). Investigation of pore structure and petrophysical property in tight sandstones. *Mar. Pet. Geol.* 91, 179–189. doi:10.1016/j.marpetgeo.2017.12.024

Lai, J., Wang, G., Fan, Z., Zhou, Z., Chen, J., and Wang, S. (2018b). Fractal analysis of tight shaly sandstones using nuclear magnetic resonance measurements. *AAPG Bull.* 102 (2), 175–193. doi:10.1306/0425171609817007

Lai, J., Wang, G., Wang, Z., Chen, J., Pang, X., Wang, S., et al. (2018c). A review on pore structure characterization in tight sandstones. *Earth-Science Rev.* 177, 436–457. doi:10.1016/j.earscirev.2017.12.003

Lala, A. M. S., and El-Sayed, N. (2017). Controls of pore throat radius distribution on permeability. *J. Pet. Sci. Eng.* 157, 941–950. doi:10.1016/j.petrol.2017.08.005

Li, X., Wang, Y., and Lin, W. (2022). Micro-pore structure and fractal characteristics of deep shale from wufeng formation to longmaxi formation in jingmen exploration area, hubei Province. *Nat. Gas. Geosci.* 33 (4), 629–641. doi:10.1016/j.jnggs.2022.06.001

Liu, B., He, S., Meng, L., Fu, X., Gong, L., and Wang, H. (2021). Sealing mechanisms in volcanic faulted reservoirs in xujiaweizi extension, northern Songliao Basin, northeastern China. *AAPG Bull.* 105 (8), 1721–1743. doi:10.1306/03122119048

Liu, J., Zhu, Y., and Li, Z. (2009). Characteristics and controlling factors of volcanic reservoir of Carboniferous in Santanghu Basin. *Lit. Res.* 21 (3), 23–28. doi:10.3969/j.issn.1673-8926.2009.03.005

Liu, T., Jia, H., Ji, H., Li, C., Yu, J., Jiang, Z., et al. (2022). Volcanic reservoirs lacking a paleoweathering crust in Carboniferous deposits of the Junggar Basin, western China: characteristics, controlling factors and hydrocarbon potential. *J. Petroleum Sci. Eng.* 219, 111119. doi:10.1016/j.petrol.2022.111119

Ma, B., Cao, Y., and Jia, Y. (2017). Feldspar dissolution with implications for reservoir quality in tight gas sandstones: evidence from the Eocene Es4 interval, Dongying Depression, Bohai Bay Basin, China. *J. Pet. Sci. Eng.* 150, 74–84. doi:10.1016/j.petrol.2016.11.026

Mandelbrot, B. B. (1975). Les objects fractals. *Adv. Math.* 22 (1), 129. doi:10.1016/0001-8708(76)90143-2

McKinley, J., Atkinson, P. M., Lloyd, C. D., Ruffell, A. H., and Worden, R. (2011). How porosity and permeability vary spatially with grain size, sorting, cement volume, and mineral dissolution in fluvial Triassic sandstones: the value of geostatistics and local regression. *J. Sediment. Res.* 81 (12), 844–858. doi:10.2110/jsr.2011.71

Meng, Z., Sun, W., Liu, Y., Luo, B., and Zhao, M. (2021). Effect of pore networks on the properties of movable fluids in tight sandstones from the perspective of multitechniques. *J. Pet. Sci. Eng.* 201, 108449. doi:10.1016/j.petrol.2021.108449

Pang, X., Wang, G., Kuang, L., Li, H., Zhao, Y., Li, D., et al. (2022). Insights into the pore structure and oil mobility in fine-grained sedimentary rocks: the Lucaogou Formation in Jimusar Sag, Junggar Basin, China. *Mar. Petroleum Geol.* 137, 105492. doi:10.1016/j.marpetgeo.2021.105492

Qiao, J., Zeng, J., Jiang, S., Zhang, Y., Feng, S., Feng, X., et al. (2020a). Insights into the pore structure and implications for fluid flow capacity of tight gas sandstone: a case study in the upper paleozoic of the Ordos Basin. *Mar. Petroleum Geol.* 118, 104439. doi:10.1016/j.marpetgeo.2020.104439

Qiao, J., Zeng, J., Ma, Y., Jiang, S., Feng, S., and Hu, H. (2020b). Effects of mineralogy on pore structure and fluid flow capacity of deeply buried sandstone reservoirs with a case study in the Junggar Basin. *J. Pet. Sci. Eng.* 189, 106986. doi:10.1016/j.petrol.2020.106986

Qu, Y., Sun, W., Tao, R., Luo, B., Chen, L., and Ren, D. (2020). Pore–throat structure and fractal characteristics of tight sandstones in Yanchang Formation, Ordos Basin. *Ordos Basin. Mar. Pet. Geol.* 120, 104573. doi:10.1016/j.marpetgeo.2020.104573

Qu, Y., Sun, W., Wu, H., Huang, S., Li, T., Ren, D., et al. (2022). Impacts of pore-throat spaces on movable fluid: implications for understanding the tight oil exploitation process. *Mar. Petroleum Geol.* 137, 105509. doi:10.1016/j.marpetgeo.2021.105509

Schutter, S. (2003). Hydrocarbon occurrence and exploration in and around igneous rocks. *Geol. Soc. Lond. Spec. Publ.* 214, 7–33. doi:10.1144/gsl.sp.2003.214.01.02

Shan, X., Mu, H., Liu, Y., Li, R., Zhu, J., Shi, Y., et al. (2023). Subaqueous volcanic eruptive facies, facies model and its reservoir significance in a continental lacustrine basin: a case from the Cretaceous in Chaganhua area of southern Songliao Basin, NE China. *DEVELOP* 50 (4), 826–839. doi:10.1016/s1876-3804(23)60431-8

Singh, A., Jha, N. K., Mandal, P. P., Esteban, L., and Desai, B. G. (2022). Pore throat characterization of bioturbated heterogeneous sandstone, Bhuj Formation, Kachchh India: an integrated analysis using NMR and HPMI studies. *J. Pet. Sci. Eng.* 211, 110221. doi:10.1016/j.petrol.2022.110221

Tang, H., Wang, L., Wu, H., Hu, J., Dai, X., Goh, T. L., et al. (2023). Possible geological interpretation of the volcanic seismic facies based on volcanostratigraphy elements: a case analysis of the Yingcheng Formation in the Changling Fault Depression, Songliao Basin, NE China. *Geoenergy Sci. Eng.* 225, 211668. doi:10.1016/j.geoen.2023.211668

Tian, W., Lu, S., Li, J., Wang, W., and Wen, Z. (2022). Insights into the pore structure and pore development pattern of subaqueous volcanic rocks in the Santanghu Basin, western China. *Mar. Petroleum Geol.* 135, 105387. doi:10.1016/j.marpetgeo.2021.105387

Tian, W., Lu, S., and Wang, W. (2019). Evolution mechanism of micro/nano-scale pores in volcanic weathering crust reservoir in the Kalagang Formation in Santanghu Basin and their relationship with oil-bearing property. *Oil Gas. Geol.* 40 (6), 1281–1294. doi:10.11743/ogg20190612

Wang, J., Wu, S., Li, Q., Zhang, J., and Guo, Q. (2020a). Characterization of the pore-throat size of tight oil reservoirs and its control on reservoir physical properties: a case study of the Triassic tight sandstone of the sediment gravity flow in the Ordos Basin, China. *J. Petroleum Sci. Eng.* 186, 106701. doi:10.1016/j.petrol.2019.106701

Wang, L., Li, W., and Lin, T. (2010). A comparative analysis of submarine eruptive and subaerial eruptive volcaniclsatic reservoir on characteristics of reservoir and reservoir forming dominated factors:Taking Carboniferous volcaniclsatic reservoir in Santanghu Basin as example. *Chin. J. Geol.* 45 (4), 1088–1097.

Wang, R., Shi, W., Xie, X., Zhang, W., Qin, S., Liu, K., et al. (2020b). Clay mineral content, type, and their effects on pore throat structure and reservoir properties: insight from the Permian tight sandstones in the Hangjinqi area, north Ordos Basin, China. *Mar. Petroleum Geol.* 115, 104281. doi:10.1016/j.marpetgeo.2020.104281

Wang, S., Lin, T., and Sun, P. (2012). Influences of diagenetic effects on volcanic rock reservoirs under two different sedimentary environments. *Pet. Geol. Exp.* 34 (2), 145–152. doi:10.11781/sysydz201202145

Wu, H., Ji, Y., Liu, R., Zhang, C., and Chen, S. (2017). Insight into the pore structure of tight gas sandstones: a case study in the Ordos basin, NW China. *Energy Fuel* 31, 13159–13178. doi:10.1021/acs.energyfuels.7b01816

Wu, H., Liu, R., and Ji, Y. (2016). Classification of pore structures in typical tight sandstone gas reservoir and its significance: a case study of the He8 Member of Upper Palaeozoic Shihezi Formation in Ordos Basin, China. *Nat. Gas. Geosci. in Chin.* 27 (5), 835–843. doi:10.11764/j.issn.1672-1926.2016.05.0835

Xiao, D., Jiang, S., Thul, D., Lu, S., Zhang, L., and Li, B. (2018). Impacts of clay on pore structure, storage and percolation of tight sandstones from the Songliao Basin, China: implications for genetic classification of tight sandstone reservoirs. *Fuel* 211, 390–404. doi:10.1016/j.fuel.2017.09.084

Xiao, D., Lu, S., Lu, Z., Huang, W., and Gu, M. (2016). Combining nuclear magnetic resonance and rate-controlled porosimetry to probe the pore-throat structure of tight sandstones. *Pet. explor. Dev.* 43 (6), 1049–1059. doi:10.1016/s1876-3804(16)30122-7

Xiao, D., Lu, S., Yang, J., and Zhang, L. (2017). Classifying multiscale pores and investigating their relationship with porosity and permeability in tight sandstone gas reservoirs. *Energy Fuel* 31, 9188–9200. doi:10.1021/acs.energyfuels.7b01487

Yang, X., Wang, H., Zhang, H., Wang, J., Shi, N., Zhang, H., et al. (2023). Evolutionary characteristics and key controlling factors of the volcanic rocks in the Lower Cretaceous Changling fault depression, Songliao Basin, China. *Mar. Petroleum Geol.* 153, 106263. doi:10.1016/j.marpetgeo.2023.106263

Yao, Y., Liu, D., Tang, D., Tang, S., and Huang, W. (2008). Fractal characterization of adsorption-pores of coals from North China: an investigation on CH4 adsorption capacity of coals. *Int. J. Coal Geol.* 73, 27–42. doi:10.1016/j.coal.2007.07.003

Yu, Y., Xu, H., Bai, Y., Niu, W., Tian, L., and Zhang, H. (2023). CT-based 3D pore-fracture network analysis of volcanic reservoirs of Lower Cretaceous Yingcheng formation in southern Songliao Basin, China: impact on natural gas migration. *Geoenergy Sci. Eng.* 223, 211581. doi:10.1016/j.geoen.2023.211581

Zang, Q., Liu, C., Awan, R., Yang, X., Li, G., Wu, Y., et al. (2022). Occurrence characteristics of the movable fluid in heterogeneous sandstone reservoir based on fractal analysis of NMR data: a case study of the Chang 7 Member of Ansai Block, Ordos Basin, China. *J. Pet. Sci. Eng.* 214, 110499. doi:10.1016/j.petrol.2022.110499

Zhang, J., Han, D., and Lin, W. (2024). Pore structure and fractal characteristics of coal-bearing cretaceous nenjiang shales from Songliao Basin, northeast China. *Nat. Gas. Geosci.* 35 (1), 119–132. doi:10.1016/j.jnggs.2024.03.005

Zhang, J., Tang, Y., He, D., Sun, P., and Zou, X. (2020). Full-scale nanopore system and fractal characteristics of clay-rich lacustrine shale combining FE-SEM, nano-CT, gas adsorption and mercury intrusion porosimetry. *Appl. Clay Sci.* 196, 105758. doi:10.1016/j.clay.2020.105758

Zhang, L., Lu, S., Xiao, D., and Li, B. (2017). Pore structure characteristics of tight sandstones in the northern Songliao Basin, China. *Mar. Pet. Geol.* 88, 170–180. doi:10.1016/j.marpetgeo.2017.08.005

Zhang, P., Lu, S., Zeng, Z., Chang, X., Li, J., Chen, G., et al. (2021). Pore structure and fractal character of lacustrine oil-bearing shale from the dongying Sag, bohai bay basin, China. *Geofluids* 2021, 1–19. doi:10.1155/2021/9945494

Zhang, Q., Liu, Y., Wang, B., Ruan, J., Yan, N., Chen, H., et al. (2022a). Effects of pore-throat structures on the fluid mobility in chang 7 tight sandstone reservoirs of longdong area, Ordos Basin. *Mar. Petroleum Geol.* 135, 105407. doi:10.1016/j.marpetgeo.2021.105407

Zhang, S., Yan, J., Hu, Q., Wang, J., Tian, T., Chao, J., et al. (2019). Integrated NMR and FE-SEM methods for pore structure characterization of shahejie shale from the dongying depression, bohai bay basin. *Mar. Petroleum Geol.* 100, 85–94. doi:10.1016/j.marpetgeo.2018.11.003

Zhang, Z., Yu, H., Chen, H., and Du, S. (2022b). Quantitative characterization of fracture-pore distribution and effects on production capacity of weathered volcanic crust reservoirs: insights from volcanic gas reservoirs of the Dixi area, Junggar Basin, Western China. *Mar. Petroleum Geol.* 140, 105651. doi:10.1016/j.marpetgeo.2022.105651